

Lawrence Berkeley National Laboratory

LBL Publications

Title

Impacts of Mixed-Wettability on Brine Drainage and Supercritical CO₂ Storage Efficiency in a 2.5-D Heterogeneous Micromodel

Permalink

<https://escholarship.org/uc/item/9s25k8v1>

Authors

Chang, Chun
Kneafsey, Timothy J
Wan, Jiamin
et al.

Publication Date

2020-04-29

DOI

10.1029/2019wr026789

Peer reviewed

1 Impacts of Mixed-Wettability on Brine Drainage and
2 Supercritical CO₂ Storage Efficiency in a 2.5-D
3 Heterogeneous Micromodel

4

5 Chun Chang*, Timothy J. Kneafsey, Jiamin Wan, Tetsu K. Tokunaga, Seiji
6 Nakagawa

7

8 Energy Geosciences Division, Lawrence Berkeley National Laboratory,
9 Berkeley, CA 94720, USA.

10

11

12

13 *Corresponding author. *E-mail address*: chunchang@lbl.gov

14

15

16

17

18

19

20

21

22

23

24 Key points

- 25 1. We created two mixed-wet systems with varying water- and
26 intermediate-wet patches in a 2.5-D heterogeneous micromodel;
- 27 2. The uniformly distributed intermediate-wet patches yield
28 bridging flow topology and highest storage efficiency after
29 drainage;
- 30 3. The heterogeneously distributed intermediate-wet patches
31 enhance channelized CO₂ flow and hinder storage efficiency after
32 drainage.

33 **Abstract:** Geological carbon storage (GCS) involves unstable drainage
34 processes, the formation of patterns in a morphologically unstable
35 interface between two fluids in a porous medium during drainage. The
36 unstable drainage processes affect CO₂ storage efficiency and plume
37 distribution, and can be greatly complicated by the mixed-wet nature
38 of rock surfaces common in hydrocarbon reservoirs where supercritical
39 CO₂ (scCO₂) is used in enhanced oil recovery. We performed scCO₂
40 injection (brine drainage) experiments at 8.5 MPa and 45 °C in
41 heterogeneous micromodels, two mixed-wet with varying water- and
42 intermediate-wet patches, and one water-wet. The flow regime
43 changes from capillary fingering through crossover to viscous fingering
44 in the micromodels of same pore geometry but different wetting
45 surfaces at displacement rates with $\log Ca$ (capillary number)
46 increasing from -8.1 to -4.4 . While the mixed-wet micromodel with
47 uniformly distributed intermediate-wet patches yields ~ 0.15 scCO₂
48 saturation increase at both capillary fingering and crossover flow
49 regimes ($-8.1 \leq \log Ca \leq -6.1$), the one heterogeneous wetting to scCO₂
50 results in ~ 0.09 saturation increase only at the crossover flow regime
51 ($-7.1 \leq \log Ca \leq -6.1$). The interconnected flow paths in the former are
52 quantified and compared to the channelized scCO₂ flow through
53 intermediate-wet patches in the latter by topological analysis. At
54 $\log Ca > -6.1$ (near well), the effects of wettability and pore geometry
55 are suppressed by strong viscous force. Both scCO₂ saturation and

56 distribution suggest the importance of wettability on CO₂ storage
57 efficiency and plume shape in reservoirs, and capillary leakage through
58 caprock at GCS conditions.

59

60 **1. Introduction**

61 Geological carbon storage (GCS) in subsurface reservoirs has
62 significant capacity for reducing greenhouse gas emissions into the
63 atmosphere (IPCC, 2005). Key questions include (1) the storage
64 efficiency of a geological formation, which is the fraction of the total
65 pore space used by GCS (Bachu et al., 2007; Goodman et al., 2011),
66 and (2) the spread of a CO₂ plume, which needs to be monitored and
67 controlled to ensure safe and permanent storage (Nordbotten et al.,
68 2005; Juanes et al., 2010; Doughty et al., 2010; MacMinn et al., 2010,
69 2011). Both questions are closely related to the migration of the CO₂
70 plume during injection, with formation brine (the wetting fluid)
71 displaced by supercritical CO₂ (scCO₂, the non-wetting fluid). One of the
72 major reasons for inefficient CO₂ storage in the subsurface is unstable
73 displacement characterized by fingering flow due to the low viscosity
74 of scCO₂ relative to formation brine (typical ratio ~1:20) (Zhang et al.,
75 2011a,b; Wang et al., 2012; Berg & Ott, 2012). The unstable
76 displacement and fingering flow of scCO₂ will also increase leakage
77 potential through caprock (Tsang et al., 2008), non-equilibrium CO₂
78 dissolution (Chang et al., 2013, 2014, 2016, 2017, 2019a,b), and
79 mineral trapping (Sanchez-Vila et al., 2007; Huq et al., 2015) after
80 injection ceases.

81 Unstable displacement can be further complicated by the solid
82 surface wettability. While deep saline aquifers for GCS typically show

83 water-wet behavior, depleted hydrocarbon reservoirs, where scCO₂ has
84 been used for enhanced oil recovery and carbon sequestration, can
85 exhibit intermediate-wet or mixed-wet rock surfaces (Salathiel, 1973;
86 Anderson, 1987a,b). It also has been observed the scCO₂-induced
87 wettability changes from water-wet to intermediate-wet on rock
88 surface (Yang et al., 2008; Broseta et al., 2012; Jung & Wan, 2012;
89 Seyyedi et al., 2015), in glass micromodels (Kim et al., 2015), and in
90 glass beads and sand pack columns (Tokunaga et al., 2013; Wang &
91 Tokunaga, 2015; Lv et al., 2017). These changes occur in local patches
92 where water films are thin and ionic strengths are high, yielding a
93 mixed-wet system (Kovscek et al., 1993; Jung & Wan, 2012). Many
94 studies have investigated the effects of uniform solid surface
95 wettability (from water-wet to intermediate-wet) on displacement
96 characteristics, non-wetting phase distribution and capillary trapping at
97 the reservoir scale (Al-Khdheewi et al., 2017), the core scale (e.g.,
98 Anderson, 1987a,b; Morrow, 1990; Levine et al., 2014), and the pore
99 scale (Cottin et al., 2011; Zhao et al., 2016; Hu et al., 2017a,b). At the
100 pore scale, flow dynamics of individual oil ganglions have been
101 recently imaged in a single pore/pore throat with mixed-wet solid
102 surfaces by a synchrotron-based X-ray computed tomography (Rücker
103 et al., 2019). The unstable displacement and scCO₂ saturation in
104 mixed-wet pore networks remain poorly understood, may greatly

105 complicate the modeling predictions (Celia et al., 2015), and need
106 systematic study.

107 Two-phase flow and displacement have been widely investigated
108 using two-dimensional (2-D) micromodels monitored with high-
109 resolution optical imaging systems. “2-D” here indicates the pore
110 network has varying pore sizes in the horizontal plane, but has a
111 uniform depth in the vertical dimension. The classic capillary number (Ca), in its original form: $Ca = \mu \times \bar{u} / \sigma$, was used to interpret the fingering
112 geometry in a Hele-Shaw cell by Saffman & Taylor (1958). In this
113 definition, μ is the viscosity of the resident fluid, \bar{u} is the average Darcy
114 velocity of the injected fluid, and σ is the interfacial tension between
115 the injected and resident fluid. Given negligible influences of
116 gravitational forces in thin micromodels, the classic Ca , along with the
117 viscosity ratio (M) defined as the ratio of viscosities of the displacing
118 (non-wetting) and displaced (wetting) fluids, were used to characterize
119 the pore-scale regimes of stable displacement, capillary fingering,
120 viscosity fingering, and their crossover. Different types of micromodels
121 have been developed to investigate the two-phase displacement
122 fundamentals that include (1) homogeneous pore networks composed
123 with regular cubic, cylindrical, elliptical and hexagonal posts (Xu et al.,
124 1998; Ferer et al., 2004; Cottin et al., 2010; Zhang et al., 2011a,b;
125 Wang et al., 2012; Armstrong & Berg, 2013; Chang et al., 2019a,b), (2)
126 heterogeneous pore networks with irregular cylindrical posts (Zarikos

128 et al., 2018), (3) statistically generated pore networks with or without
129 spatial correlation of pore sizes (Tsakiroglou & Avraam, 2002), and (4)
130 heterogeneous pore networks fabricated from a section micrograph of
131 natural consolidated sandstone (Zuo et al., 2013) and transparent cells
132 packed with unconsolidated, single-layered glass beads (Moebius & Or,
133 2014). Some other studies have reported better description of the
134 pore-scale viscous and capillary forces using modified Ca that
135 considers the length scales corresponding to the size of non-wetting
136 phase clusters (Hilfer & Øren, 1996; Armstrong et al., 2014; Chang et
137 al., 2019a). Common to all of the above studies is the use of 2-D
138 geometry of pore network that has a constant pore/pore throat depth.
139 Lacking ability to continuously record in-situ and dynamic interfacial
140 curvature, measured pore widths and depths were used to calculate
141 the capillary pressure using Young-Laplace equation. The dependence
142 of this relation on the sum of the inverse of two orthogonal radii of
143 curvatures shows that constant-depth micromodels effectively fix one
144 of the principal radii, thus limiting the range of capillary pressures
145 achievable through variation of pore widths. The pioneering work from
146 Wan et al. (1996) improved the glass micromodel design and
147 fabrication to provide the necessary contrast of depths (thus
148 capillarity) between matrix pores and fracture apertures. In recent
149 years, more 2.5-D micromodels have been used to better mimic real 3-
150 D porous media and investigate multiphase flow (Park et al., 2015; Yun

151 et al., 2017; Xu et al., 2017a,b). To our best knowledge, there are few
152 studies on unstable drainage processes in micromodels having 2.5-D
153 pore geometry heterogeneity, especially for GCS applications, and
154 none that have examined impacts of mixed wetting.

155 In this study, we (1) create mixed-wet systems by heterogeneously
156 applying octadecyltrichlorosilane (OTS, 0.2% by vol. in hexane) flow to
157 modify surface wettability of a 2.5-D micromodel in two ways, (2)
158 investigate the scCO₂ displacement characteristics and compare the
159 steady-state scCO₂ saturations for water-wet and the two types of
160 mixed-wet micromodels; and (3) quantify the scCO₂ flow
161 characteristics at both pore- and pore-network scale through a
162 topological analysis. We conducted a series of experiments by injecting
163 scCO₂ into an initially brine-saturated micromodel at displacement
164 rates resulting in $\log Ca$ (logarithm of the capillary number) ranging
165 from -8.1 to -4.4 , allowing investigation of capillary through viscous
166 fingering (at constant $M = 0.038$). For simplicity and ease of
167 comparisons with other studies, the first form of the capillary number
168 Ca used in this presentation does not include a contact angle term.
169 Later, the capillary number Ca^i containing the cosine of the effective
170 contact angle will be introduced for comparison. Images of scCO₂ and
171 water distribution were obtained at appropriate junctures to provide
172 direct observations on the pore-scale displacement characteristics and

173 scCO₂ saturation in these pore networks having heterogeneity in both
174 2.5-D pore geometry and surface wettability.

175 **2. Materials and methods**

176 **2.1 2.5-D micromodel**

177 Figure 1(a) shows the 2.5-D pore network contained in a 20 mm
178 ×10 mm rectangle, with a porosity of 0.43 and pore volume of 3.44 μL.
179 The pore network, with pore space shown in white and solid posts in
180 black, was extracted from micro-CT images of sand pack of irregular
181 shaped sand grains, then etched on two symmetrical silica wafers with
182 hydrofluoric acid and then fused together (Micronit Microfluidics BV,
183 Netherlands). The different depths of pores and pore throats were
184 created through etching two mirror image networks, both to 20 μm
185 depths, but with one face having locations left unetched. Thus, 40 μm
186 depth pores are created at locations where both faces were etched to
187 20 μm, while 20 μm deep throats were created at locations where only
188 one face was etched. Direct aligned bonding of the two plates was then
189 performed by creating a prebond between the two wafers, which was
190 then annealed at high temperature. Given the strong bonding, the
191 micromodel can be operated under the pressure difference (inside
192 relative to outside) up to 10 MPa, without applying any confining
193 pressure as has been required in other high-pressure micromodels
194 (Zhang et al., 2011a; Chang et al., 2016). Figure 1(b) shows the 2-D
195 pore-size distribution (without taking into account the depth of the

196 micromodel) characterized by a local thickness plugin in ImageJ
 197 software (Hildebrand and Rüesgsegger, 1996; Rasband, 1997–2019).
 198 The average pore and pore-throat size are 190 and 48 μm ,
 199 respectively, while the average post size is 290 μm .

200 The pore network also contains a capillary barrier transverse to the
 201 flow direction (marked by the yellow lines in Figure 1(a) and 1(c)),
 202 composed by a line of tight pore throats 20 μm deep. Figure 1(d)
 203 depicts the capillary entry pressure along the capillary barrier,
 204 calculated from the pore/pore throat size and depth as follows:

205
$$p_b = \frac{\sigma \cos\theta (r_1 + r_2)}{r_1 r_2} \quad \text{Eq. (1)}$$

Fluid properties		Displacement rate		
Pressure	8.5 MPa	Q ($\mu\text{L}/\text{min}$)	\bar{u} (m/d)	$\log Ca$
Temperature	45 °C	0.1	0.8	-8.1
Viscosity scCO ₂ /water (mPa·s)	0.023/0.597	0.5	4.2	-7.4
Viscosity Hexane/EG (mPa·s)	0.30/16.90	1.0	8.4	-7.1
Interfacial tension (mN/m)	28.5	2.0	16.7	-6.8
Micromodel properties		5.0	41.9	-6.4
Dimension (cm ²)	2.0 × 1.0	10	83.7	-6.1
Pore volume (μL)	3.44	20	167.4	-5.8
Porosity	0.43	50	418.6	-5.4
Pore/throat depth (μm)	40/20	100	837.2	-5.1
Pore/throat/post diameter (μm)	190/48/290	200	1674.4	-4.8
scCO ₂ /water contact angle	27°	500	4186.0	-4.4

206 where $\sigma = 28.5$ mN/m (Chiquet et al., 2007), θ is measured as 27° for
 207 scCO₂ and brine (see Section 3.1 for more details), r_1 is the local pore
 208 radius quantified from Figure 1b and r_2 is the half pore depth. Although

209 40 μm deep pores are distributed throughout the micromodel, as
210 shown in Figure 1(c) and 1(d), there are only eight of these pores along
211 A-A' (marked by the red arrows), with the others being 20 μm deep.
212 These eight locations will be referred to as "slots" because they
213 constitute pores with low capillary entry pressures. The impacts of this
214 unique characteristic on scCO_2 invasion patterns for water-wet and
215 mixed-wet conditions will be presented in Section 3. Table 1 lists more
216 details on the pore network.

217

218 Table 1. Summary of experimental conditions, fluid and micromodel
219 properties, volumetric flow rates, and corresponding Darcy velocities
220 and capillary numbers

221

222

223

224

225

226

227

228 **Figure 1.** (a) Pore characteristics of the 2.5-D micromodel used in this
229 study, with solid posts shown in black, large pores 40 μm deep shown
230 in white and tight pore throats 20 μm deep in red. (b) The pore size
231 distribution quantified by the Local Thickness plugin in ImageJ

232 software. (c) The sub-image magnified from the red box in (a) that
233 shows the transverse capillary barrier in the pore network. (d) The
234 capillary entry pressure of pores and pore throats for scCO₂-water
235 displacement with water-wet solid surface ($\theta = 27^\circ$) along the yellow
236 dotted line A-A' shown in (a) and (c). S1 to S8 (marked by the red
237 arrows in (c)) are the open slots in the capillary barrier with reduced
238 capillary entry pressure that may provide potential flow paths for CO₂
239 invasion. The blue box in (a) and (c) bounds the local pore domain that
240 correlates to the narrow intermediate-wet choke point in Figure 3(c)
241 and constrained scCO₂ flow in Figure 4(b). The blue arrow indicates the
242 scCO₂ flow direction during the displacement experiments.

243

244 **2.2 Mixed-wet treatment**

245 Contacting the water-wet glass surface with octadecyltrichlorosilane
246 (OTS) strongly impacts the wettability, changing it towards non-water
247 wetting. The coating solution was prepared by diluting
248 octadecyltrichlorosilane (Cole-Parmer, IL) with hexane (ACS grade,
249 Cole-Parmer, IL) in 4.0%, 0.4% and 0.2% volumetric fractions. Before
250 modifying wettability of the glass micromodel, treatment tests on glass
251 microscope slides were conducted following the sequential steps of (1)
252 acid cleaning, (2) coating in OTS/hexane solution, (3) rinsing in hexane
253 to remove excess OTS, and (4) drying in oven at 100 °C. Contact angle
254 measurements of a water droplet on the microscope slides show

255 values change from 0° to $\sim 75^\circ$ after treatment by the three
256 concentrated solutions. The contact angle remains constant for over 2
257 years, indicating the long-term effectiveness of the method (Figure S1
258 of the supporting information (SI)). The lowest concentrated (0.2% v/v)
259 OTS solution was selected for micromodel treatment to minimize
260 potential effects from the excess OTS. A similar OTS/hexane solution
261 has also been used for changing glass surface wettability in a previous
262 study (Goodwin et al., 2016).

263 To create a mixed-wet system in the micromodel, we used the OTS/
264 hexane solution as the invading fluid into an ethylene glycol (EG,
265 wetting phase) saturated micromodel. During the treatment, we were
266 able to easily observe the two-phase interface and wettability-altered
267 pore domain because we colored the EG with sulphorhodamine B and
268 collected images of dyed EG distribution under UV light. A low dye
269 concentration (0.23 g/L) was used to minimize its potential effect on
270 fluid viscosity, while allowing sufficient optical detection for phase
271 discernment. The viscosities of the coating solution and dyed EG were
272 assumed equal to that of hexane (0.3 mPa·s) and EG (16.9 mPa·s) due
273 to the low OTS and dye concentration, while the interfacial tension
274 (IFT) between hexane and dyed EG at ambient conditions was
275 measured as 20.5 mN/m through a high-precision tensiometer (Kruss,
276 Germany). Note the close viscosity ratio and IFT between hexane-EG
277 under ambient conditions and scCO_2 -water system under designated

278 experimental conditions (at 8.5 MPa and 45°C, $\mu_{CO_2} = 0.02$ mPa·s,
279 $\mu_{brine} = 0.6$ mPa·s, IFT: 28.5 mN/m). With these similarities, the mixed-
280 wet pattern induced by hexane-based coating solution and EG was
281 expected to be similar to that induced by scCO₂-brine at GCS
282 conditions. This was experimentally validated and is presented in
283 Sections 3.2 and 3.3.

284 During treatment, the micromodel was first acetone cleaned, air
285 dried and then saturated with dyed EG. The surface coating OTS
286 solution was then injected at constant flow rates using a syringe pump
287 (Harvard Apparatus, Holliston, MA). Over 3 and 300 pore volumes (PVs)
288 of coating solution were injected into the micromodel at 3 μ L/hour (
289 $\log Ca = -7.2$) and 6000 μ L/hour ($\log Ca = -3.9$), respectively, until the
290 two-phase distribution in the pore network remained constant with
291 time. After ten displacement experiments with varying injection rates
292 between them using hexane and EG, we selected the minimum and
293 maximum rate injections, which represent potential mixed-wet
294 patterns induced by capillary fingering (minimum rate injection) and
295 viscous fingering (maximum rate injection). Other mixed-wet patterns
296 may vary between them, but we think these two are the boundary
297 cases that worth of detailed investigation. The coating solution
298 injection ceased after soaked for over 20 min in the pore network,
299 followed by 100 PVs of hexane injection to remove excess OTS from
300 the pore network. Finally, the micromodel was air-dried and cured in

301 the oven at 100° for 1 hour, similar to the treatment on microscope
302 glass slides. Fluorescent images were acquired to characterize the
303 mixed-wet patterns using a Sony FDR-AX100 camcorder with a spatial
304 resolution of 4.5 μm/pixel.

305 **2.3 Experimental setup and procedures**

306 A high-pressure, elevated-temperature setup (Figure 2) was built
307 based on Hu et al. (2017b) for scCO₂ displacement experiments in the
308 water-wet and two mixed-wet micromodels. To establish the initially
309 brine-saturated conditions, low pressure gaseous CO₂ was first injected
310 into the micromodel to displace air from the micromodel and tubing. It
311 should be noted that, to avoid corrosion, our “brine” was a low salinity
312 solution (0.01 M NaCl). This brine was then injected from the back-
313 pressure pump to displace and dissolve the gaseous CO₂ through
314 E→D→C→B→F→H. During these steps, the micromodel system was kept
315 at atmospheric pressure. Similar low salinity brine was also used by Hu
316 et al. (2017b), with an aim to minimize any wettability changes
317 induced by salinity and ionic composition (Fathi et al., 2010,
318 Karadimitriou et al., 2019).

319 The scCO₂ pump was initially filled with wet CO₂ at approximately
320 5.87 MPa from a source tank (99.99% purity, Airgas) while Valve A
321 connecting scCO₂ pump to the micromodel was closed. The scCO₂
322 pump was then pressurized up to 8.5 MPa. The pressure in the
323 micromodel and pipeline E→D→C→B→F→G was gradually increased to

324 8.5 MPa using the back-pressure pump filled with brine, while keeping
325 valve G connecting to the brine pump closed. All fluids were then
326 allowed to equilibrate at 45 °C for over 12 hours. The pressure and
327 temperature represent reservoir conditions at depths of about 1.0 km.

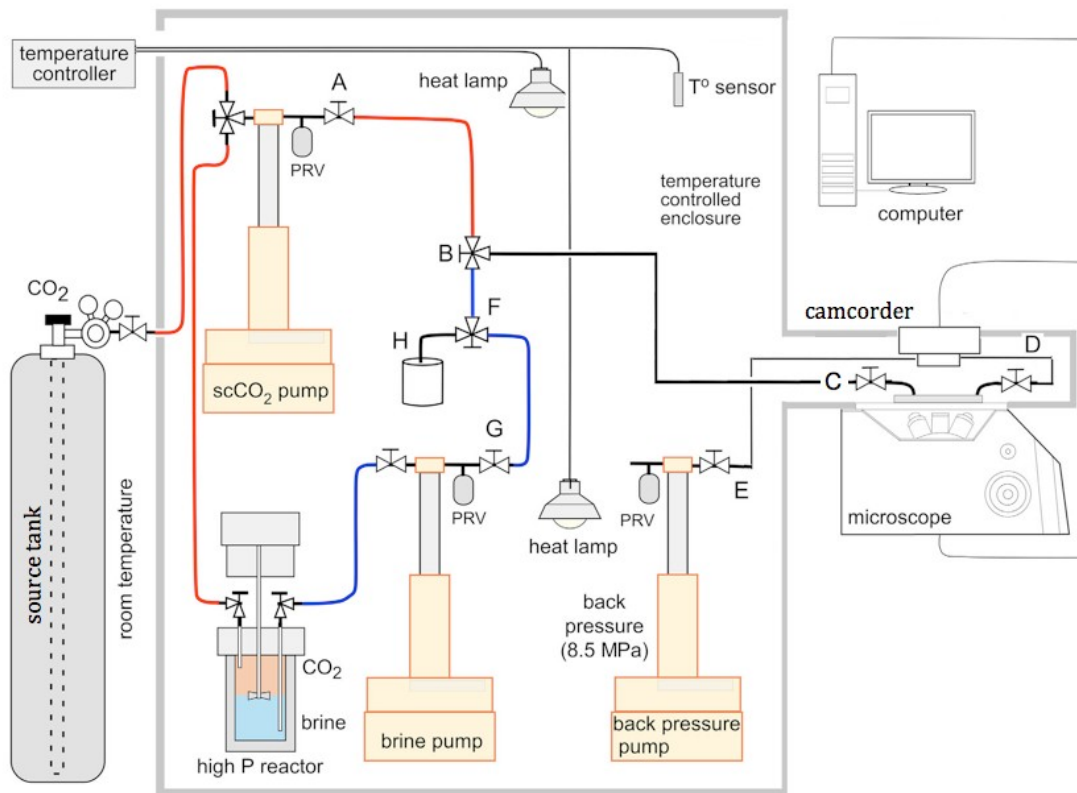
328 To prepare the mutually saturated brine and scCO₂, 200 mL brine
329 was first injected into the high-pressure reactor (see Figure 2), and
330 then pressurized up to 8.5 MPa by CO₂ injection. The reactor containing
331 scCO₂ and brine was heated up to 45 °C and stirred for 24 hours. The
332 scCO₂-saturated brine was then transferred to the brine pump. Over
333 100 PVs of scCO₂-saturated brine was then injected to completely
334 saturate the micromodel and the pipelines through G→F→B→C→D→E.
335 Displaced fluid was collected in the back-pressure pump, and the
336 micromodel and fluid delivery pipelines were kept constant at 8.5 MPa
337 and 45 °C.

338 After the above steps were completed, pre-wetted scCO₂ in the
339 scCO₂ pump was injected into the micromodel at a specific constant
340 flow rate. Displaced brine was collected in the back-pressure pump,
341 which was maintained at a constant withdrawal rate matched to that of
342 the scCO₂ injection. In this way, we obtained good experimental
343 reproducibility under the exactly same experimental conditions (see
344 more details in Figure S2 of SI). When the quasi-steady state was
345 reached, i.e., scCO₂ distribution and saturation remained constant with
346 time, scCO₂ injection was stopped. The micromodel was then flooded

347 with scCO₂-saturated brine until no scCO₂ was observed, to prepare the
348 micromodel for the next experiment, conducted at a different scCO₂
349 injection rate. This sequence was repeated for a wide range of flow
350 rates. To avoid any contamination effects on the pore surface
351 wettability during the displacement tests, no dye was employed in
352 either the scCO₂ or brine. Table 1 lists the imposed volumetric injection
353 rates in the three micromodels. These rates correspond to a range of
354 Darcy velocities from 0.84 m/day to 4190 m/day, and a range of *logCa*
355 from -8.1 to -4.4. The imposed range of injection rates correspond to
356 flow rates at 0.02 to 70 m away from a typical injection well (with an
357 injection rate of one million metric tonnes of scCO₂ per year over a
358 screen length of 15 m assuming uniform flow) at a GCS site.

359 Despite complications that can arise from scCO₂-induced wettability
360 alteration such as those noted in the Introduction, we do not expect
361 considerable wettability changes on micromodel surfaces subjected to
362 repeated scCO₂ injection because of the relative short time of scCO₂
363 presence in the micromodel (aging time from minutes to hours), and
364 the low ionic strength (0.01M NaCl) used in brine. Hu et al. (2017a,b)
365 also reported constant contact angle measurements before and after
366 repeated scCO₂ injection tests, using the same type of silica
367 micromodel (differing only in pore geometry), similar experimental
368 setup, and the same experimental pressure, temperature and brine
369 salinity. Significant wettability changes from brine acidification after

370 scCO₂ dissolution may not be expected from (1) Hu et al. (2017a,b)
371 mentioned above, and (2) Gribanova et al. (1976) who reported that as
372 pH decrease from 6 to 3, contact angles only slightly increased from
373 19° to 23° in the air–brine–silica system (Gribanova et al., 1976).
374 Nevertheless, it should be recognized that solid surfaces in reservoirs
375 are composed of diverse minerals, where non-uniform chemical
376 interactions (both mineral dissolution and precipitation) and changes of
377 electrochemical properties at brine-rock interface occur, inducing
378 mixed-wet surfaces. These can be further enhanced by the non-
379 uniform scCO₂ dissolution and mass transfer in brine, as previously
380 reported (Chang et al., 2017, 2019a). Results from Wang et al. (2013)
381 showed large contact angle variation on different pure mineral
382 surfaces, and analysis suggested that the 38% differences in degrees
383 of contact angle reported could manifest in 5–10% differences in
384 capillary trapping or pressure. In this study, we further show the
385 considerable changes of scCO₂ saturation after drainage by the mixed-
386 wet solid surface.



387 **Figure 2.** Schematic of the experimental setup for scCO₂ injection and
 388 brine drainage tests.

389

390 **2.4 Image analysis**

391 Imaging was performed using an inverted microscope (Carl Zeiss,
 392 Observer Z1.m) equipped with a CCD camera (Carl Zeiss, Axiocam
 393 MRc5) that records images at the pore scale, and a Sony FDR-AX100
 394 4K camcorder installed over the stage of the inverted microscope to
 395 record images at the pore-network scale. Segmentation and analysis of
 396 the images were conducted using ImageJ - public domain JAVA based
 397 software (Rasband, 1997-2019). Because efficient and direct

398 segmentation of scCO₂ from brine and solid posts is difficult, the
399 following steps were applied to the raw images: the raw images taken
400 during a displacement test were first subtracted from the image taken
401 at the initially water-saturated condition, followed by a median and a
402 bilateral filtering (Chaudhury et al., 2011) of the resulting images. A
403 threshold value was then unambiguously determined for each image to
404 distinguish scCO₂ phase from others. More details on the process and
405 superimposed image comparing the contours before and after
406 segmentation are presented in Figure S3 of the SI. We manually drew
407 the contour of the scCO₂ phase in the original subdomain (3.8 × 3.7
408 mm², as shown in Figure S3(a), also identical to Figure 5(d)) and
409 calculated the pore space area occupied by scCO₂. By comparison with
410 the segmented image in Figure S3(d), we showed errors < 1%, which
411 mostly originated from the edges and connectivities in the narrow pore
412 throats. The resulting binary images were then used to present the
413 displacement characteristics and calculate scCO₂ saturation in the
414 water-wet and two mixed-wet micromodels.

415 **3. Results and discussion**

416 In this section, we first present the contact angle measured for
417 scCO₂-brine and mixed-wet patterns after coating treatment in Section
418 3.1, followed by scCO₂ saturation and distribution at injection rates
419 varying from $\log Ca = -8.1$ to -4.4 in the water-wet and two mixed-
420 wet 2.5-D micromodels in Sections 3.2 and 3.3. In Section 3.4, we

421 further quantify the flow characteristics and topological scCO₂
422 distribution in different micromodels at the pore- and pore-network
423 scale. In Section 3.5, the classic *logCa* -*logM* diagram is presented and
424 the impacts of pore geometry and mixed-wettability are discussed. We
425 finally discuss the experimental implications on spatial variations of
426 CO₂ saturation in a typical GCS site in Section 3.6.

427 **3.1 Contact angle and mixed-wet patterns after treatment**

428 The contact angle was measured for scCO₂-brine at 8.5 MPa and
429 45°C. Both of the untreated water-wet and treated mixed-wet
430 micromodel were initially brine-saturated, followed by scCO₂ injection
431 at a low rate until the scCO₂-brine distribution in the micromodel was
432 stable with time. The valves connecting to the inlet and outlet of the
433 micromodel were then closed for 12 hours, and microscope images
434 were taken at different locations of the pore network to measure
435 scCO₂-brine contact angles on solid posts. Menisci of scCO₂-brine
436 interface were selected such that each meniscus possessed a flat
437 contact line of sufficient length so that the change in post geometry
438 and surface roughness did not considerably affect the contact angle
439 measurements. Figure 3(a) presents an example of the microscope
440 image showing the variability of contact angle between scCO₂ (white)
441 and brine (gray) in the treated micromodel (marked by the white
442 dashed rectangle in Figure 3(d)). Within the local pore network domain
443 of 2.6×1.9 mm², the contact angle varies considerably, from 27° to

444 119°, indicating a mixed-wet system. This wide variation in contact
445 angle is attributed to the non-uniform flow of coating solution during
446 treatment. Bypassed patches filled by EG may retain originally water
447 wet where coating is difficult to establish. Figure 3(b) further compares
448 the contact angles obtained from over 60 menisci selected within the
449 entire pore network. In the untreated micromodel, the values vary
450 from 20° to 35°. With an average value of $27^\circ \pm 4^\circ$, the untreated
451 micromodel shows a strong water-wet surface, similar to that reported
452 by Hu et al. (2017b), who measured the average contact angle of
453 scCO₂-brine at 20° in a micromodel made of the same silica glass. It
454 should be noted that their silica posts were fabricated with circular and
455 smooth surfaces. The slightly higher contact angle measured in our
456 micromodel may be attributed to the rough surface of the glass posts
457 and associated contact line pinning. Figure 3(b) also shows
458 considerable increases in the average contact angle and variations of
459 contact angles after coating treatment. The contact angles after
460 treatment vary from 34° to 145°, with an average value of $89^\circ \pm 28^\circ$.
461 Note the menisci were selected over the entire pore network. This
462 variation in contact angle indicates the spatial heterogeneity in
463 wettability, ranging from strongly water-wet to strongly CO₂-wet
464 (Iglauer et al., 2015). This pore space heterogeneous wetting to brine
465 results in different scCO₂ invasion characteristics, which are presented
466 in detail in Section 3.3.

467 **Figure 3.** (a) A microscope image showing wide varieties of contact
468 angles between scCO₂ (white) and brine (gray) within a local pore
469 domain (indicated by the white dashed rectangle in (d)) after OTS
470 treatment. (b) The contact angle measurements from over 60 selected
471 menisci within the pore network for both untreated and treated
472 micromodels. The quasi-steady state distribution of dyed EG (red
473 color) in the micromodel after OTS injection at (c) $\log Ca = -7.2$, and (d)
474 $\log Ca = -3.9$. OTS coating solution was injected from the left side of the
475 micromodel as indicated by the blue arrow. The white arrow in (c)
476 denotes the narrow intermediate-wet choke point established after
477 OTS treatment.

478

479 Note that we measured the contact angle of menisci where both
480 scCO₂ and brine were present. We assume the wettability of pore
481 space invaded by coating solution during treatment is altered to non-
482 wetting, and that saturated with EG retains its original water-wet
483 surface characteristic. The assumptions were supported through
484 measuring over 60 scCO₂-brine menisci present within the pore space
485 previously invaded by the coating solution or saturated by EG (see
486 Figure 3b). We will provide more evidence and discussion by
487 comparing the mixed-wettability patterns vs. CO₂ distribution in
488 Section 3.4.

489 The distributions of dyed EG (red color) after treatment are shown
490 in Figure 3(c) and 3(d), while the invaded coating solution and silica
491 posts are presented non-fluorescent in blue to black color. The
492 saturation of coating solution in the pore network is 0.50 and 0.70 at
493 low (Figure 3(c)) and high (Figure 3(d)) injection rate, resulting in
494 different areas that had wetting-altered pore surfaces. The average
495 length and standard deviation of EG clusters after area-weighted in
496 Figure 3(c) were measured as 2560 μm and 1870 μm , while the values
497 are $\sim 1/3$ at 870 μm and 596 μm in Figure 3(d). It should be noted that
498 when the OTS solution advanced beyond the capillary barrier, it
499 channeled through the relatively open pore domain outlined by the
500 blue frame (Figures 1a. and 1c). By making the pore surfaces in this
501 more open domain intermediate-wet, it became a location where
502 invading scCO_2 flow was focused after passing through the capillary
503 barrier. Once through this location, scCO_2 flow diverged as discussed
504 later. Thus, this intermediate-wet region behaves as a choke point for
505 scCO_2 invasion (see more details in Section 3.3).

506 The treated and untreated water-wet (WW) micromodels with
507 identical geometry were then used in the scCO_2 injection tests. For
508 simplicity, we define (1) the capillary mixed-wet (CM) micromodel as
509 the model was established at a low injection rate of coating solution
510 (Figure 3(c)), where the intermediate-wet patches were capillary-force
511 induced and heterogeneously distributed in the pore network; and (2)

512 the viscous mixed-wet (VM) micromodel as the model was established
513 at a high injection rate of coating solution (Figure 3(d)), where the
514 intermediate-wet patches were viscous-force induced and uniformly
515 distributed in the pore network.

516 **3.2 scCO₂ saturation and distribution in the 2.5-D water-wet** 517 **(WW) micromodel**

518 Figure 4(a) shows the quasi-steady state scCO₂ distributions after
519 displacement in the WW micromodel. The corresponding displacement
520 rates ($\log Ca$) and CO₂ saturations are presented in the parentheses.
521 Depending on injection rates, the injected scCO₂ volumes at steady
522 state range from 3 PVs at $\log Ca = -8.1$ to 200 PVs at $\log Ca = -4.4$. The
523 overall scCO₂ flow characteristics with varying displacement rates are
524 distributed across the classic fingering regimes, i.e., capillary fingering
525 dominates at low displacement rate ($\log Ca < -6.4$), where scCO₂ flows
526 in forward and lateral flow paths with large clusters of entrapped
527 water; viscous fingering develops at large displacement rate ($\log Ca >$
528 -6.1), where scCO₂ widely invades the pore network and displaces
529 water in the form of multiple narrow and well-connected flow paths. At
530 intermediate rates ($\log Ca = -6.4$ and -6.1), crossover from capillary to
531 viscous fingering is shown by the coexistence of distributed capillary
532 fingering (near the upstream) and concentrated viscous fingering (near
533 the downstream), similar to the experimental observations from Wang

534 et al. (2012), Ferer et al. (2004) and pore-network simulations by
535 Lenormand et al. (1988).

536 Differing from above studies in a 2-D micromodel, however, we
537 observe the great impacts of 2.5-D heterogeneity of pore geometry on
538 scCO₂ distribution. As shown in Figure 4(a) and for most cases ($\log Ca$
539 < -5.1), scCO₂ invades the open slots (marked by the white circles) of
540 the transverse barrier (see Figure 1(a)) that are close to the top and
541 bottom boundaries, and bypasses the barrier and even some slots in
542 center (marked by the red circles). The half-depth barrier hinders
543 longitudinal scCO₂ flow in the center and enhances transverse flow that
544 bypasses the slots in front. We selected a local pore domain located by
545 the red box in Figure 4(a) to better understand and discuss the scCO₂
546 flow in Section 3.4.1. At $\log Ca \geq -5.1$, scCO₂ invades most of the slots
547 under the strong viscous force. The capillary blockage of scCO₂ and
548 flow direction changes at a local pore domain are enhanced by the
549 depth-reduced pore throat, comparing to that in a 2-D micromodel that
550 possesses a constant pore throat depth.

551 **3.3 scCO₂ saturation and distribution in the 2.5-D mixed-wet** 552 **micromodels**

553 The fingering flow patterns and CO₂ saturations in the two mixed-
554 wet micromodels are presented in Figures 4(b) and 4(c). The classic
555 flow regime transition from capillary fingering through crossover to
556 viscous fingering can also be observed. At low injection rates ($\log Ca =$

557 -8.1 and -7.4), CO_2 saturations are ~ 0.65 and ~ 0.50 in the VM and
558 CM micromodel, but at the crossover zone ($\log \text{Ca} = -6.4$), the values
559 decrease to 0.49 and 0.42 . Further increasing the injection rates in both
560 micromodels results in continuous increase of CO_2 saturations to a
561 similar value of 0.80 at maximum $\log \text{Ca} = -4.4$. The dependence of CO_2
562 saturation on solid surface wettability can be deduced from the 30
563 displacement tests in the three micromodels. For instance, at low
564 injection rates where the flow regime is dominated by capillary
565 fingering ($-8.1 \leq \log \text{Ca} < -6.4$), CO_2 saturation in the VM micromodel
566 is 0.12 to 0.14 higher than that in the WW micromodel (see Figures 4(a)
567 and 4(c)), while the value in the CM micromodel is 0.03 lower at $\log \text{Ca}$
568 $= -8.1$, and 0.05 to 0.07 higher at $\log \text{Ca} = -7.1$ and -6.8 . The
569 saturation enhancement reaches maximum of 0.18 and 0.12 in the VM
570 and CM micromodels at the intermediate-rate injections, where the flow
571 regime is dominated by crossover from capillary to viscous fingering (
572 $\log \text{Ca} = -6.4$ and -6.1). At higher rates ($\log \text{Ca} > -6.1$), the effect of
573 wettability and pore geometry is suppressed by strong viscous force,
574 resulting in high CO_2 saturation in the three micromodels at the
575 maximum injection rate. The overall higher CO_2 saturation in the two
576 mixed-wet micromodels at $\log \text{Ca} \leq -6.1$ is attributed to the lower
577 capillary entry pressure in pore networks having solid surfaces more
578 wetting to the displacing scCO_2 , similar to previous observations from
579 Cottin et al. (2011), Zhao et al. (2016) and Hu et al. (2017a).

580 We show in Figure 4 that more CO₂ saturation enhancement occurs
581 in the VM micromodel than that in the CM. In the two micromodels
582 having identical pore geometry, the lower saturation enhancement in
583 the CM micromodel can be attributed to effectively less area converted
584 to hydrophobic surfaces relative to the VM micromodel. These
585 converted hydrophobic surfaces, at the same time, are more
586 heterogeneously distributed within the pore network (see Figure 2(a)
587 and 2(b)), resulting in higher variations of capillary entry pressure
588 among local pores/pore throats. The heterogeneously distributed
589 hydrophobic surfaces then enhance channelized scCO₂ flow and hinder
590 scCO₂ displacement efficiency. The non-uniform displacement and
591 preferential CO₂ flow in micromodels and rock cores subject to pore-
592 and sub-core scale heterogeneity has been extensively reported
593 (Krevor, et al., 2011; Shi et al., 2011; Pini et al., 2012; Berg & Ott,
594 2012; Berg et al., 2013; Chang et al., 2013, 2014; Chen et al., 2018). In
595 a previous study, we presented in four centimeter-scale micromodels
596 the change of CO₂ saturations by a factor of ~10 at similar imposed
597 displacement rates, depending on the heterogeneity and anisotropy of
598 pore networks (Chang et al., 2019b). We show here the importance of
599 mixed wettability and its effect on displacement efficiency and CO₂
600 saturation, particularly at low displacement rates. In reservoirs where
601 the flow rate is relatively slow ($Ca < 10^{-7}$) and displacement is
602 dominated by capillary fingering, CO₂ storage efficiency may be

603 collectively dependent on pore geometry, solid surface wettability and
604 their heterogeneity.

605 Different CO₂ distributions in the two mixed-wet pore network are
606 also shown in Figure 4. In the CM micromodel and at $\log Ca < -4.4$, the
607 open slots invaded and bypassed by scCO₂ were spatially mixed (see
608 the mixed white and red circles in Figure 4(b)), differing from that in
609 the WW micromodel (see Figure 4(a)). More importantly, at
610 intermediate-rate injections ($-6.8 \leq \log Ca \leq -5.4$), we observed a
611 single scCO₂ flow path developed at the barrier downstream (marked
612 by the white arrows in Figure 4(b)). Lower and higher injection rates
613 resulted in additional flow paths around it. This single flow path
614 gradually developed into several dendritic paths towards the outlet.
615 The unique scCO₂ flow pattern can be attributed to the preferential
616 scCO₂ flow through the narrow intermediate-wet (instead of
617 geometrically induced) choke point marked by the white arrow in
618 Figure 2(a) and bounded by the blue rectangles in Figure 1(a) and 1(c).
619 In the VM micromodel with more uniformly distributed intermediate-wet
620 patches, scCO₂ broadly invaded the pore network with well-connected
621 flow paths, except for a bypassed water body at the bottom left corner
622 (see Figure 4(c) at $\log Ca < -6.1$). No significant blockage from the
623 transverse capillary barrier was observed, regardless of flow rate.

624 **Figure 4.** The quasi-steady state scCO₂ (shown in green) distribution
625 after displacement in the micromodel of (a) water-wet (WW), (b)

626 capillary mixed-wet (CM) and (c) viscous mixed-wet (VM). The numbers
627 in the parentheses are $\log Ca$ values and CO_2 saturations, respectively.
628 $scCO_2$ is injected at the left side of these images, as indicated by the
629 blue arrow. The circles refer to the open slots in Figure 1c invaded
630 (white) and bypassed (red) by $scCO_2$. The white arrows in (b) indicate
631 the constrained $scCO_2$ flow induced by the narrow intermediate-wet
632 choke point. The red boxes in (a), (b) and (c) mark the local pore
633 domains selected for analyzing pore-scale drainage characteristics and
634 mixed-wettability effects in Figure 5 at $\log Ca = -6.4$.

635

636 In addition to the local choke point, we compare the mixed-wet
637 patterns vs. $scCO_2$ distribution in the entire pore network by
638 overlapping Figure 4(b) at $\log Ca = -8.1$, -6.1 and -4.4 with Figure
639 3(c), and Figure 4(c) at $\log Ca = -8.1$, -6.1 and -4.4 with Figure 3(d).
640 The resulting images (see more details in Figure S4 of the SI) show
641 70% of $scCO_2$ in the CM pore network distributes within the
642 intermediate-wet patches at $\log Ca = -8.11$, while the value in the VM
643 pore network is 60%, indicating a more uniform CO_2 distribution among
644 the water-wet and intermediate-wet patches. Both values decrease
645 with increasing injection rates to 50% at $\log Ca = -4.4$, when compact
646 invasion dominates under strong viscous force regardless of
647 heterogeneities in surface wettability and pore geometry. We do not
648 expect or see exactly the same flow patterns even under the same

649 experimental conditions, as the randomness of pore size and grain
650 surface, as well as the randomness of interfacial velocity at local pores/
651 pore throats (Kataok et al., 1986). Most of the time we use (lumped)
652 saturation, pressure data and statistics (e.g., the skeleton analysis
653 here) to investigate the fundamental processes. We think we have
654 sufficient reproducibility to distinguish the different flow regimes and
655 mixed-wet impacts as shown by Figure S2 of the SI.

656 **3.4 Quantifications on scCO₂ flow characteristics**

657 In this section, we quantify the scCO₂ flow characteristics that were
658 descriptive in previous studies (e.g., Lenormand, et al., 1988; Zhang et
659 al, 2011b; Wang et al., 2012), and discuss the effects of mixed-
660 wettability at both pore and pore-network scales. The pore-scale
661 analysis focuses on a local pore domain at $3.8 \times 3.7 \text{ mm}^2$ in vicinity of
662 the capillary barrier (indicated by the red squares in Figure 4).
663 Quantification of the pore-network-scale flow characteristics was
664 applied to all the displacement tests in the three micromodels.

665 *3.4.1 Pore-scale scCO₂ flow characteristics*

666 Figure 5(a) depicts the selected local pore domain composed of (1)
667 ~100 solid posts (shown in black), (2) large pores 40 μm deep (shown
668 in yellow) and (3) tight pore throats 20 μm deep (shown in red). The
669 average pore and pore-throat size is measured as 204 μm and 80 μm ,
670 respectively from Figure 5(g). The porosity is 0.44, similar to the entire

671 pore network. Figure 5(d) represents the scCO₂ flow paths (in white
672 color) after displacement within the WW domain at $\log Ca = -6.4$. As
673 shown in the figure, scCO₂ invades the pore domain from the top left
674 and the bottom right corner (see the red arrows), transversely flows
675 through the domain along the red dotted arrows and flows out of the
676 domain along the blue arrows. Note the bulk flow direction is from left
677 to right. The blockage of scCO₂ by the capillary barrier occurs, resulting
678 in flow direction changes and bypass of tight (only 20 μm deep) pore
679 throats. After injection, CO₂ saturation in the WW domain is stable at
680 0.43. The OTS-altered intermediate-wet patches and CO₂ distribution in
681 the CM and VM domains are also compared for $\log Ca = -6.4$, and
682 shown in white in Figures 5(b), 5(c), and Figures 5(e) and 5(f),
683 respectively. The steady-state CO₂ saturation after displacement is
684 0.43 and 0.62, respectively in the CM and VM domain, among which
685 90% and 64% distributes within the intermediate-wet patches.

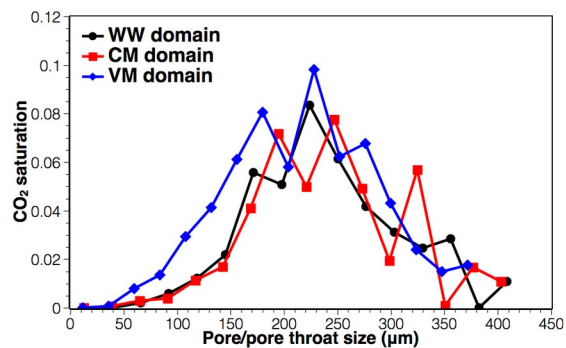
686 The mixed-wettability changes the scCO₂ saturation distribution vs.
687 pore/pore throat size in Figure 5(h), which is obtained from aligning
688 Figure 5(d), 5(e) and 5(f) with Figure 5(g). For all the three domains,
689 the majority of scCO₂ distributes in large pores/pore throats at 80 to
690 400 μm , with less than 1% in the tight pore throats ($< 80 \mu\text{m}$ diameter
691 and 20 μm deep). The tight pore throats account for 3% of the pore
692 space in the domain and the pore network. We also observe (1) similar
693 correlations in the WW and CM domains, while a higher CO₂ saturation

694 distribution occurs in smaller pores ($< 200 \mu\text{m}$ diameter) in the VM
695 domain (the accumulative CO_2 saturation in these small pores is 0.29
696 in the VM domain, while the value is 0.15 in the WW and CM); (2)
697 larger saturation variations in large pores ($>300 \mu\text{m}$) in the CM domain
698 (note the more irregular red plot). These are consistent with Figure
699 5(d), 5(e) and 5(f), and indicate different topologies of scCO_2 flow path,
700 i.e., better interconnections of flow in large and small pores/pore
701 throats in the VM domain, and more constrained flow in the CM domain
702 with bypass of small pore throats and even large pores.

703 Characterizing scCO_2 distribution topology is important for
704 understanding its invasion into pore networks and ultimately to help
705 predict scCO_2 plume shape in reservoirs. We apply a skeleton analysis
706 in the same local pore domain using an Analyze Skeleton plugin in
707 ImageJ to better quantify the topology of scCO_2 flow paths and impacts
708 of mixed-wettability. The skeleton geometry is defined as a thin
709 version of that geometry which is equidistant to its boundaries. The
710 binary images of scCO_2 phase in the three types of pore domains
711 (Figures 5 (d), (e), (f)) are first skeletonized in ImageJ and illustrated by
712 branches and junctions shown in Figure 5(i), 5(j) and 5(k). A branch is
713 composed of slab pixels that have exactly 2 neighbor pixels, while a
714 junction is defined as the intersection of multiple (more than two)
715 branches, i.e., the junction pixels have more than 2 neighbors. More
716 details on the terminology and method are provided in Arganda-

717 Carreras et al. (2010). The numbers of branches and junctions, as well
718 as the average branch length for scCO₂ flow paths were calculated and
719 listed in Table 2. Also shown in Table 2 are values for the pore domain.
720 The branch numbers increase from 61 in the CM to 135 in the WW, and
721 reach maximum at 221 in the VM domain. Correspondingly, the
722 junction number increases from 29 in the CM to 67 in the WW, and
723 reaches maximum at 110 in the VM domain. Conversely, the average
724 branch length is shortest in the VM and longest in the CM domain.
725 These indicate a more interconnected flow topology of scCO₂ after
726 displacement in the VM domain, and a more channelized scCO₂ flow in
727 the CM domain. The average branch length of scCO₂ flow paths in the
728 WW domain is 226 μm, which is close to the value of the pore domain
729 (240), indicating a flow characteristic dominated by pore geometry.

731 **Figure 5.** scCO₂ flow characteristics and mixed-wet effects through a
732 topological skeleton analysis over a local pore domain (3.8 × 3.7 mm²).
733 (a) Pore characteristics of the originally WW domain, with full-depth (40
734 μm) pores shown in yellow and half-depth (20 μm) pore throats in red
735 (these color indicators are also applied to (b), (c), (d), (e) and (f)). (b)
736 and (c) show the **scCO₂ distribution** mixed-wet patterns in the
737 CM and VM domains, with water-wet
738 pore space shown in yellow and intermediate-wet pore space in white.
739 (d), (e) and (f) present the quasi-steady state scCO₂ (in white)
740 distribution in the WW, CM and VM domains, respectively. The red
741 dotted arrows indicate the scCO₂ flow directions within the domain,
742 along with red solid arrows for
743 entrance and blue solid arrows
744 for exit. (g) and (h) are the
745 pore size distribution and CO₂
746 saturation distribution vs. pore/
747 pore throat size **Skeletonized scCO₂ flow path** within the pore
748 domain quantified by the Local Thickness plugin in ImageJ software.
749 (i), (j) and (k) show the skeletonized CO₂ distribution composed by
750 branches and
751 junctions in different pore domains.



752 Table 2. The branch and junction number, and average branch length
753 for scCO₂ flow at $\log Ca = -6.4$ and the selected pore domain by a
754 skeleton analysis

Topological characteristics of scCO₂ flow paths			
Wetting type	Number of branches	Number of junctions	Average branch length (μm)
CM	61 (0.22)	29 (0.18)	389 (1.62)
WW	135 (0.48)	67 (0.42)	226 (0.94)
VM	221 (0.79)	110 (0.69)	194 (0.81)
Topological characteristics of pore domain			
	280	158	240

760

761

762 Note: The numbers in the parentheses are specific values calculated
763 from ratios between scCO₂ flow paths and pore domain for Number of
764 branches, Number of junctions and Average branch length.

765

766

767

768

769

770

771

772

773

774

775

776

777

778

779

780

781

782

783

784

785

786 **Figure 6.** The specific branch and junction number, and specific

787 branch length vs. $\log Ca$ in the WW, CM and VM micromodel.

788 3.4.2 Pore-network-scale flow characteristics

789 We applied the topological analysis to the three micromodels to
790 investigate scCO₂ flow characteristics at the pore-network scale. The
791 branch and junction number, and the average branch length for scCO₂
792 flow paths (N_b, N_j and L), and for the pore networks ($N_{b,m}, N_{j,m}$ and L_m)
793 were first calculated, and their ratios, defined as specific branch
794 number, specific junction number and specific branch length are
795 presented as a function of $\log Ca$ in Figure 6. In the WW micromodel,
796 the branch and junction numbers that keep relatively high plateau
797 values at $\log Ca < -6.5$ (black lines Figure 6(a) and 6(b)) correspond to
798 the wide invasion and randomly distributed forward and lateral flow
799 paths observed in the capillary fingering regime. The considerable
800 reduction in branch and junction numbers at $\log Ca = -6.4$ and -6.1 is
801 consistent with the crossover from capillary to viscous fingering and
802 decreased displacement efficiency. At higher injection rates ($\log Ca >$
803 -6.1) where viscous fingering dominates the flow regime, the branch
804 and junction numbers increases with new developed and
805 interconnected flow paths. The variation of the specific branch length
806 as a function of $\log Ca$ (Figure 6(c)) is generally mirrored to specific
807 branch and junction number vs. $\log Ca$. This is expected as flow paths
808 develop interconnected, the branch and junction number increase
809 whereas the average branch length decreases.

810 Figure 6 also presents the largest branch and junction numbers in
 811 the VM micromodel among the three. This is in favor of GCS by
 812 increasing displacement efficiency. The CM micromodel yields longest
 813 branch length and lowest branch and junction number. In mixed-wet
 814 caprocks, the channelized flow developed within the intermediate-wet
 815 patches may increase capillary leakage of scCO₂ accumulation below
 816 because of the locally reduced capillary entry pressure.

817 **3.5 CO₂ saturation vs. capillary number considering mixed** 818 **wettability**

819 Figure 7(a) presents the relations between CO₂ saturation and *logCa*
 820 for the displacement experiments conducted in the three wetting types
 821 of micromodels. An alternative definition of capillary number (Ca^i) from
 822 Lenormand et al. (1988) that considers the solid surface wettability is
 823 calculated as follows:

$$824 \quad Ca^i = (\mu \times \bar{u}) / (\sigma \times \acute{c}os\theta), \quad \text{Eq. (2)}$$

825 Where $\acute{c}os\theta$ is derived from the pore space area (*A*) and average
 826 contact angle of the water-wet and intermediate-wet patches:

$$827 \quad \acute{c}os\theta = \frac{A_1 \cos\theta_1 + A_2 \cos\theta_2}{A_1 + A_2} \quad \text{Eq. (3)}$$

828 For the CM micromodel, $\theta_1 = 27^\circ$, $A_1 / (A_1 + A_2) = 0.50$; $\theta_2 = 89^\circ$, $A_2 / (A_1 + A_2)$
 829 $= 0.50$; for the VM micromodel, $\theta_1 = 27^\circ$, $A_1 / (A_1 + A_2) = 0.30$; $\theta_2 = 89^\circ$,
 830 $A_2 / (A_1 + A_2) = 0.70$. For the original WW micromodel, $\theta_1 = \theta_2 = 27^\circ$. The

831 CO₂ saturation vs. $\log Ca^i$ relations for the three micromodels are
832 shown by colored plots in Figure 7(a), which translate rightward from
833 the CO₂ saturation - $\log Ca$ relations at 0.4 unit in the CM and 0.6 unit
834 in the VM micromodel. In the WW micromodel, the two plots overlap
835 without considerable change due to the small contact angle. These
836 correspond to the fact that the presence of intermediate-wet rock
837 surfaces (larger contact angles) further assures viscous fingering
838 within the near-field network and transition to the capillary fingering
839 regime occurs closer to the injection well. The Ca^i that consider solid
840 surface wettability may be able to better quantify the fingering and
841 crossover flow regimes. However, caution is needed as variations of
842 contact angles and their spatially heterogeneous distributions are
843 likely to be more complex in natural reservoirs formations than in the
844 two treated micromodels.

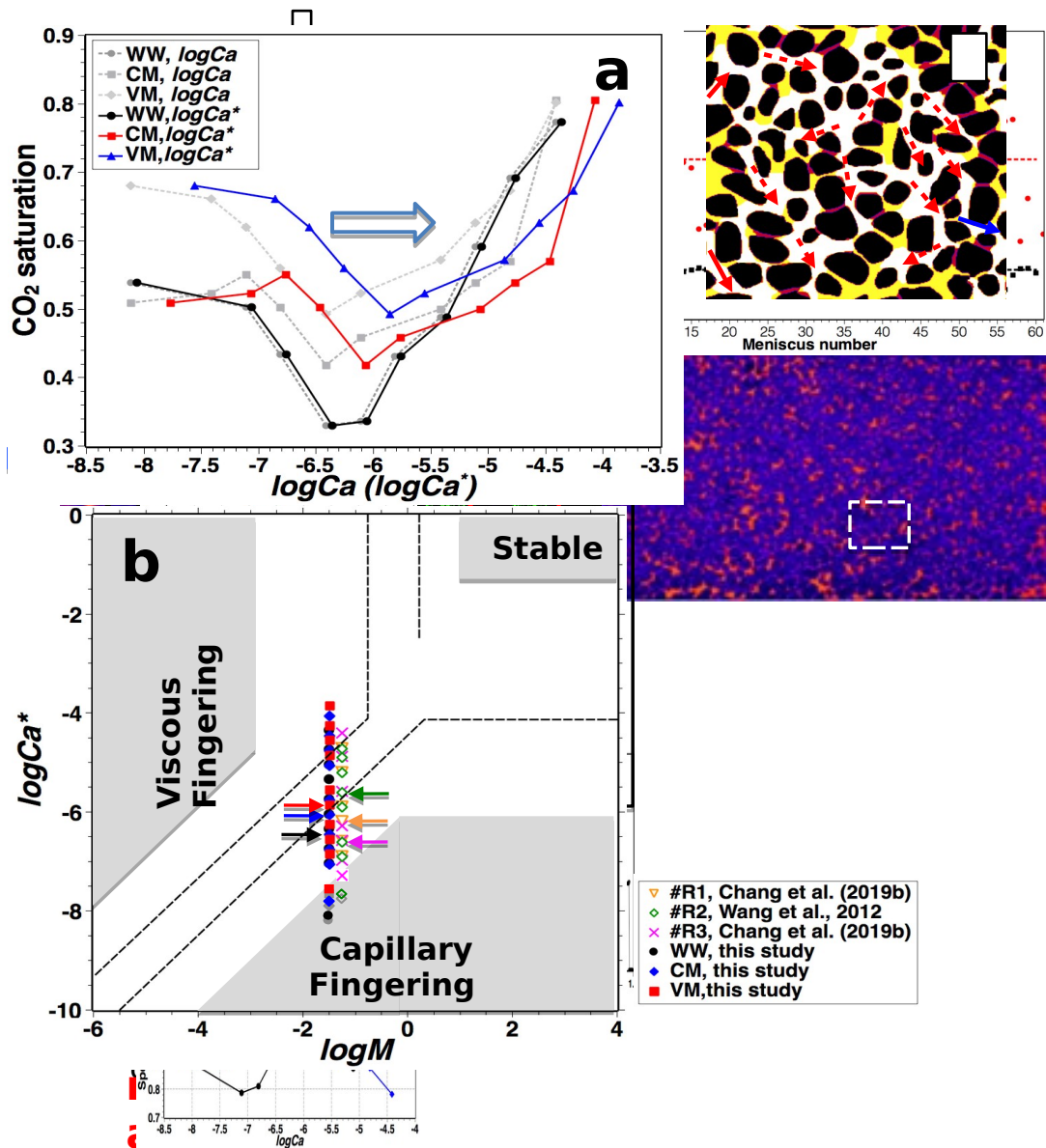
845 Figure 7(b) illustrates the classic $\log Ca^i$ - $\log M$ diagram, with
846 boundaries of different displacement patterns from Lenormand et al.
847 (1988) shown in gray and Zhang et al. (2011) in dash lines. The
848 different boundaries observed from the two studies were attributed to
849 the different pore geometries and pore-size variations. The values of
850 $\log Ca^i$ and $\log M$ used in this study are shown by solid symbols. In a
851 previous study (Chang et al., 2019b), we conducted scCO₂
852 displacement experiments at 40 °C and 9 MPa in (1) an anisotropic
853 and homogeneous micromodel consisting of elliptical silicon posts, with

854 estimated transverse-to-longitudinal permeability ratio of 0.63; (2) a
855 heterogeneous sandstone-analogue micromodel, which was patterned
856 based on section micrographs of a Mt. Simon sandstone core extracted
857 from the injection well of the Illinois Basin - Decatur project (Senel et
858 al., 2014). We include data on the two micromodels (hollow symbols)
859 and refer them as #R1 and #R3 in the figure. Under similar conditions
860 at 41°C and 9.0 MPa, Wang et al. (2012) conducted scCO₂
861 displacement tests in a homogeneous isotropic pore network that
862 consisted of 200 μm cylindrical silicon posts, 120 μm pore bodies and
863 26.7 μm pore throats. Their results were shown and referred as #R2 in
864 Figure 7(b) (see more detailed images on the referred micromodels in
865 Figure S5 of the SI). All the referred data were obtained in micromodels
866 with water-wet solid surfaces ($\theta=15^\circ$) and similar pore/pore throat
867 depth (35 to 37 μm). We tried to include as much data as possible for
868 better comparison, however, were hindered by the narrow capillary
869 number range applied in previous studies, particularly by the
870 deficiency at low rates ($\log Ca^i < -7.0$) that are dominant at GCS sites.

871 The colored arrows in Figure 7(b) indicate the flow regime crossover
872 with minimum CO₂ saturation observed in each study. The crossover
873 $\log Ca$ values in this and referred studies, regardless of pore
874 geometries or surface wettabilities, ranges from -5.6 to -6.6,
875 generally lower than the boundaries (-4.6 to -5.8) predicted by Zhang
876 et al. (2011) at a similar $\log M$ value of -1.34. The displacing fluid

877 (dodecane) viscosity from Zhang et al. (2011), however, is almost two
878 orders of magnitude higher at 1.35 mPa·s than that of scCO₂ used in
879 this study, while the interfacial tension (IFT) between the displacing
880 and resident fluid (polyethylene glycol 200) is lower at 13.87 mN/m.
881 The low scCO₂ viscosity and high IFT with brine may intensify
882 interfacial instability for scCO₂-brine displacement and result in lower
883 $\log Ca^c$ values for flow regime changes from capillary fingering to
884 crossover. In a 2-D homogeneous micromodel, Armstrong & Berg
885 (2013) showed that individual pore drainage events occurred at an
886 intrinsic rate, which was independent of bulk flow rate. Further
887 modeling results indicated the two-phase interfacial velocity increased
888 with decreasing viscosity of the displacing phase or increasing
889 interfacial tension and for the same capillary number, the velocity of
890 two-phase interface can differ by an order of magnitude or more
891 (Armstrong et al., 2015). The broad distribution in Ca associated with
892 crossover (minimum nonwetting phase saturation indicated by arrows
893 in Figure 7(b)) suggests that capillary number alone does not explain
894 the pore-scale displacement. While most studies focus on the fingering
895 flow regimes and transitions using fluid pairs of different viscosity
896 ratios (Dong et al., 2011; Zhang et al., 2011a,b; Dehoff et al., 2012;
897 Wang et al., 2012; Liu et al., 2013; Zheng et al., 2017), additional
898 studies are required using fluid pairs of same viscosity ratio but
899 different in displacing fluid viscosities or IFTs.

900
 901
 902
 903
 904
 905
 906
 907
 908
 909
 910
 911
 912
 913
 914
 915
 916
 917
 918



919 **Figure 7.** (a) The correlations of CO₂ saturation vs. $\log Ca$ (the
 920 gray dash lines) and CO₂ saturation vs. $\log Ca^*$ (the colored solid
 921 lines) for the displacement experiments conducted in the three wetting

922 types of micromodels. The blue arrow indicates the shift direction of
923 $\log Ca^i$ from $\log Ca$. (b) $\log Ca^i - \log M$ stability diagram showing three
924 stability areas and the locations of the displacement experiments in
925 this and previous studies for scCO₂ and water. The dash lines are the
926 stability boundaries from Zhang et al. (2011b) and the gray zones
927 denote the stability areas from Lenormand et al. (1988). The colored
928 arrows mark the conditions at saturation minimum in each study.
929

930 **3.6 Field implications**

931 The 30 tests under the wide range of displacement rates allowed
932 investigations on the full spectrum of fingering flow regimes, CO₂
933 saturations, and mixed-wettability impacts. These results have
934 implications for a GCS site. In Figure 8, we show CO₂ saturation vs.
935 distance to the injection well calculated from the typical CO₂ flow
936 velocity in a GCS site. We assume (1) at the field, CO₂ is injected at a
937 volumetric rate (Q) of 10,000 m³/d over a screen length of 15 m, and
938 (2) scCO₂ density (ρ) from reservoir pressure and temperature is close
939 to that at experimental conditions and CO₂ velocities in the formation
940 is radially uniform. This volumetric rate corresponds to an annual
941 injection of one million metric tonnes of CO₂ at 8.5 MPa and 45 °C (this
942 study), and 1.8 million metric tones of CO₂ at 9 MPa and 40 °C (Wang
943 et al., 2012; Chang et al., 2019b). The distance from the injection well
944 can then be calculated as follows:

945
$$d = \frac{Q}{2\pi h \bar{u}} \quad \text{Eq. (4)}$$

946 Where d refers to the (radial) distance to the injection well, h is the
947 screen length of the injection well, and \bar{u} is the CO₂ velocity that
948 equals to the lab values listed in Table 1.

949 Results from Wang et al. (2012) and Chang et al. (2019b) in
950 Micromodel #R1, #R2, #R3 and #R4 were also included in Figure 8,
951 with estimated CO₂ saturations from their published figures. #R4 refers
952 to an anisotropic and homogeneous micromodel that consists of
953 elliptical silicon posts with estimated transverse-to-longitudinal
954 permeability ratio of 6.86 (see Figure S5 for more details in the SI).
955 #R4 also possesses water-wet solid surface ($\theta=15^\circ$) and constant
956 pore/pore throat depth at 37 μm . CO₂ saturations after displacement in
957 this micromodel showed high values (~ 0.90) over the applied injection
958 rates, with no crossover flow observed.

959 In the three micromodels of identical geometry, CO₂ saturation
960 varies as a function of distance to the injection well, depending on the
961 wettability. Comparing to the WW micromodel, VM enhances CO₂
962 saturation over the investigated distance up to 130 m away from the
963 injection well, while CM only enhances the value at locations 0.25 to 25
964 m away. In the WW and two mixed-wet micromodels, the crossover
965 from viscous to capillary fingering occurs at locations close to the
966 injection well (1.27 to 2.50 m), and the two mixed-wet systems

967 accelerate the saturation rebound to saturation plateau. For the seven
968 micromodels investigated, viscous fingering flow dominates the
969 constrained locations < 1 m away from the injection well, imposing a
970 very limited impact on the storage efficiency at the field. This again
971 indicates that laboratory experiments at low injection rates are
972 important for obtaining more field-relevant implications.

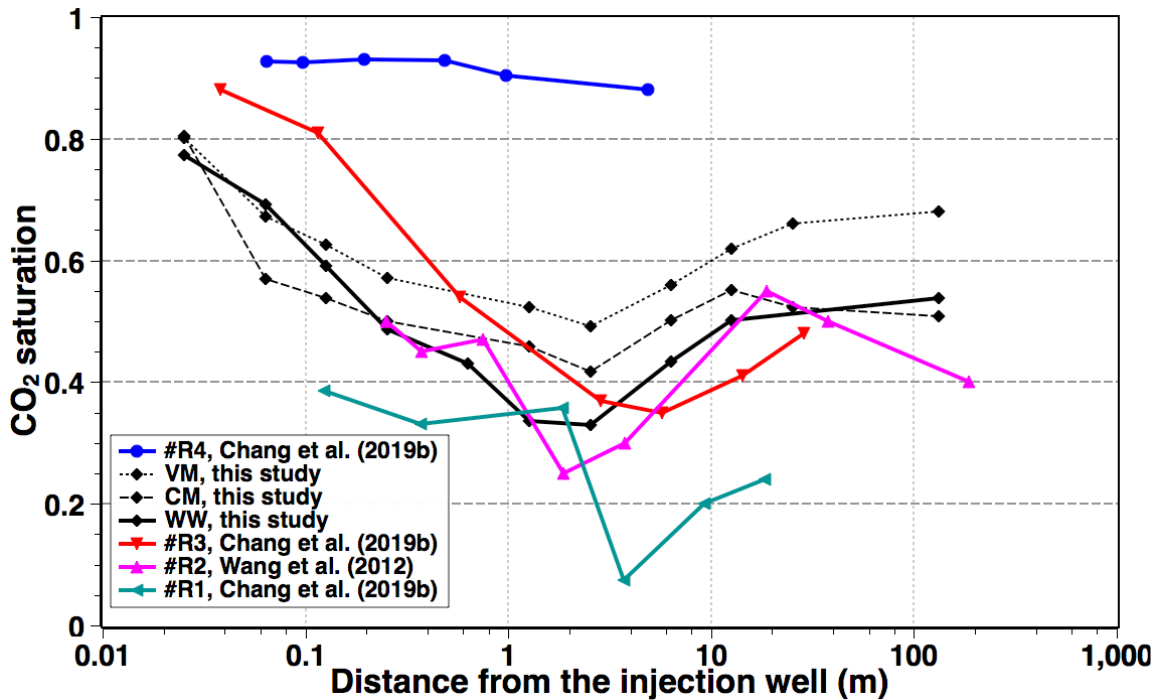
973 Figure 8 also indicates the great impact of pore-network anisotropy
974 and heterogeneity on CO₂ saturation. As shown in the figure, pore-
975 network anisotropy imposes the most pronounced effect on CO₂
976 saturation. The anisotropic Micromodel #R4 with high transverse-to-
977 longitudinal permeability ratio (6.86:1) results in highest CO₂
978 saturations, while the anisotropic Micromodel #R1 with low transverse-
979 to-longitudinal permeability ratio (0.63:1) yields lowest CO₂ saturations
980 at 0.10 to 0.40. The pore size surprisingly does not have a considerable
981 impact on CO₂ saturation at locations > 20 m away from the injection
982 well, when comparing Micromodel #R2 with Micromodel #R3 and the
983 2.5-D heterogeneous WW micromodel in this study. A higher CO₂
984 saturation was expected in Micromodel #R2 containing large 120 μm
985 pore and in the WW micromodel with an average pore size of 190 μm.
986 The average pore size of Micromodel #R3 is smaller at 33 μm. Note the
987 small pore depth relative to pore size in #R2 and the WW micromodel,
988 which may limit the displacement efficiency since (1) Wang et al.
989 (2012) observed the transition of scCO₂ flow from widely distributed

990 forward and lateral flow paths to one gradually narrowing finger
991 leading to the outlet and bypass the major pore domain by the small
992 variations of pore depth in Micromodel #R2, and (2) we observed the
993 preferential flow of CO₂ through the deep open slots in the transverse
994 capillary barrier and bypass the majority of pore domain downstream
995 in the WW micromodel. The effect of depth variation is weakened in
996 Micromodel #R3 due to the similar pore size and depth. We emphasize
997 here the importance of pore/pore throat depth in determining two-
998 phase flow and saturation, and suggest careful consideration of the
999 third dimension during micromodel design and fabrication.

1000 It is noted that results from this and previous studies were obtained
1001 in centimeter-scale micromodels that possess pore size variations in a
1002 range of tens to hundreds of micrometers. Great caution is needed in
1003 using these laboratory results for understanding field-scale GCS
1004 behavior (e.g., predicting the CO₂ saturation vs. distance to the
1005 injection well using Figure 8) because heterogeneities and gravity are
1006 important at the larger scale. In the field, the viscous/capillary scCO₂
1007 fingers may coincide with high-permeability channels developed at the
1008 meter to kilometer scale, while local pore structures and small fingers
1009 may become secondary in affecting the scCO₂ plume (Birkholzer et al.,
1010 2015). In addition, gravity could not be considered in these laboratory
1011 experiments on horizontal pore networks. The interplay between
1012 viscous/capillary fingering and gravity are also important as gravity is

1013 dominant in shaping 3-D plumes and increasing leakage potential
1014 through the caprock (Zhou & Birkholzer, 2011; Trevisan et al., 2017).

1015 **Figure 8.** CO₂ saturation vs. distance from the injection well (in
1016 logarithmic scale) for the displacement experiments conducted in the
1017 three micromodels and in Wang et al. (2012) and Chang et al. (2019b)



1018 using different pore networks under similar experimental conditions.

1019

1020 4. Conclusions

1021 Secure and efficient CO₂ storage in a geological formation can be
1022 affected by the mixed-wettability of reservoir rocks, and therefore this
1023 characteristic requires a systematic investigation. By applying a

1024 coating solution to modify wettability in a 2.5-D micromodel, we
1025 created two mixed-wet systems, one viscous force-induced resulting in
1026 uniformly distributed intermediate-wet patches; and one capillary
1027 force-induced resulting in heterogeneously distributed intermediate-
1028 wet patches. The two mixed-wet and the originally water-wet
1029 micromodels were then compared in scCO₂ injection experiments. A
1030 full spectrum of flow-regime transition from capillary fingering through
1031 crossover to viscous fingering was observed in the three micromodels.
1032 The pronounced effects of 2.5-D heterogeneity of pore network on
1033 scCO₂ distribution and saturation were indicated by (1) scCO₂
1034 preferential flow along the large 40 μm deep pores and bypass of tight
1035 20 μm deep pore throats, and (2) the comparisons between
1036 micromodels with varying pore characteristics. A detailed analysis on
1037 CO₂ saturation and topological distribution showed (1) high storage
1038 efficiency and wide interconnections of CO₂ flow paths in reservoirs
1039 containing more and uniformly distributed intermediate-wet and water-
1040 wet patches, and (2) hindered storage efficiency and channelized CO₂
1041 flow paths in reservoirs containing heterogeneously distributed
1042 intermediate-wet patches. The channelized flow of scCO₂ (especially at
1043 locations close to injection well) may increase leakage potential
1044 through caprock. This pore-network-scale study indicates the
1045 importance of mixed-wettability in determining CO₂ storage efficiency

1046 and spatial variation in depleted hydrocarbon reservoirs and others
1047 that may present mixed-wet rock surface.

1048

1049 **Supporting Information (SI)**

1050 More detailed information on the contact angle measurements,
1051 characterizations on the drainage flow regimes and referred
1052 micromodels are provided in the SI.

1053 **Conflicts of interest**

1054 The authors declare no competing financial interest.

1055

1056 **Acknowledgements**

1057 This material was based upon the work supported by the U.S.
1058 Department of Energy, Office of Science, Office of Basic Energy
1059 Sciences, Energy Frontier Research Centers program under Contract
1060 no. DE-AC02-05CH11231. We appreciate the valuable comments
1061 provided by the reviewers and the Associate Editor, which helped
1062 improve presentation of this work. Data are deposited in the Dryad
1063 repository with DOI: 10.7941/D14P62, and available through the
1064 following link during the review process:

1065 <https://datadryad.org/stash/share/>

1066 [MMmArpl0nxlOdS2jO4VF0dFWi9NLFHFB2HzoYx9EGSc.](https://doi.org/10.7941/D14P62)

1067

1068 **References**

- 1069 Al-Khdheawi, E., Vialle, S., Sarmadivaleh, M., Barifcani, A., & Iglauer,
1070 S. (2017). Impact of reservoir wettability and heterogeneity on CO₂
1071 plume migration and trapping capacity. *Int. J. Greenhouse Gas*
1072 *Control*, 58, 142–158.
- 1073 Anderson, W. G. (1987a). Wettability literature survey—part 4: effects
1074 of wettability on capillary pressure. *J. Petrol. Technol.*, 39 (10),
1075 1283-1300.
- 1076 Anderson, W.G. (1987b). Wettability literature survey Part 6: the
1077 effects of wettability on water flooding. *J. Petrol. Technol.*, 39 (12),
1078 1605-1622.
- 1079 Arganda-Carreras, I., Fernandez-Gonzalez, R., Munoz-Barrutia, A., &
1080 Ortiz-De-Solorzano, C. (2010). 3D reconstruction of histological
1081 sections: Application to mammary gland tissue. *Microsc. Res. Tech.*,
1082 73 (11), 1019-1029.
- 1083 Armstrong, R. T., & Steffen, B. (2013). Interfacial velocities and
1084 capillary pressure gradients during Haines jumps. *Phys. Rev. E*,
1085 88(4), 600-614.
- 1086 Armstrong, R. T., Georgiadis, A., Ott, H., Klemin, D., & Berg, S. (2014).
1087 Critical capillary number: desaturation studied with fast X-ray
1088 computed microtomography. *Geophys. Res. Lett.* 41, 55-60.
- 1089 Bachu, S., & Bennion, B. (2007). Effects of in-situ conditions on relative
1090 permeability characteristics of CO₂-brine systems. *Environ. Geol.*, 54

1091 (8), 1707-1722.

1092 Berg, S., & Ott, H. (2012). Stability of CO₂-brine immiscible
1093 displacement. *Int. J. Greenhouse Gas Control*, 11, 188-203.

1094 Berg, S., Oedai, S., & Ott, H. (2013). Displacement and mass transfer
1095 between saturated and unsaturated CO₂-brine systems in
1096 sandstone. *Int. J. Greenhouse Gas Control*, 12, 478-492.

1097 Birkholzer, J. T., Zhou, Q., & Tsang, C. (2009). Large-scale impact of
1098 CO₂ storage in deep saline aquifers: A sensitivity study on pressure
1099 response in stratified systems. *Int. J. Greenhouse Gas Control*, 3 (2),
1100 181-194.

1101 Birkholzer, J. T., Oldenburg, C. M., & Zhou, Q. (2015). CO₂ migration
1102 and pressure evolution in deep saline aquifers. *Int. J. Greenhouse
1103 Gas Control*, 40, 203-220.

1104 Broseta, D., Tonnet, N., & Shah, V. (2012). Are rocks still water-wet in
1105 the presence of dense CO₂ or H₂S? *Geofluids*, 12, 280-294.

1106 Chang, C., Zhou, Q., Xia, L., Li, X., & Yu, Q. (2013). Dynamic
1107 displacement and non-equilibrium dissolution of supercritical CO₂ in
1108 low permeability sandstone: An experimental study. *Int. J.
1109 Greenhouse Gas Control*, 14, 1-14.

1110 Chang, C., Zhou, Q., Guo, J., & Yu, Q. (2014). Supercritical CO₂
1111 dissolution and mass transfer in low-permeability sandstone: Effect
1112 of concentration difference in water-flood experiments. *Int. J.
1113 Greenhouse Gas Control*, 28, 328-342.

1114 Chang, C., Zhou, Q., Kneafsey, T. J., Oostrom, M., Wietsma, T. M., & Yu,
1115 Q. (2016). Pore-scale supercritical CO₂ dissolution and mass transfer
1116 under imbibition conditions. *Adv. Water Resour.*, 92: 142–158.

1117 Chang, C., Zhou, Q., Oostrom, M., Kneafsey, T. J., & Mehta, H. (2017).
1118 Pore-scale supercritical CO₂ dissolution and mass transfer under
1119 drainage conditions, *Adv. Water Resour.*, 100, 14–25.

1120 Chang, C., Zhou, Q., Kneafsey, T. J., Oostrom, M., & Ju, Y. (2019a).
1121 Coupled supercritical CO₂ dissolution and water flow in pore-scale
1122 micromodels. *Adv. Water Resour.*, 123, 54–69.

1123 Chang, C., Kneafsey, T. J., Zhou, Q., Oostrom, M., & Ju, Y. (2019b).
1124 Scaling the impacts of pore-scale characteristics on unstable
1125 supercritical CO₂-water drainage using a complete capillary number.
1126 *Int. J. Greenhouse Gas Control*, 86, 11–21.

1127 Chaudhury, K. N., Sage, D., & Unser, M., (2011). Fast O(1) bilateral
1128 filtering using trigonometric range kernels, *IEEE Trans. Image*
1129 *Process*, 2(12), 3376–3382.

1130 Chen, Y., Li, Y., Valocchi, A. J., & Christensen, K. T. (2018). Lattice
1131 Boltzmann simulations of liquid CO₂ displacing water in a 2D
1132 heterogeneous micromodel at reservoir pressure conditions. *J.*
1133 *Contam. Hydrol.*, 212, 14–27.

1134 Chiquet, P., Daridon, J. L., Broseta, D. & Thibeau, S. (2007). CO₂/water
1135 interfacial tensions under pressure and temperature conditions of
1136 CO₂ geological storage. *Energy Convers. Manage.*, 48, 736–744.

- 1137 Cihan, A., Birkholzer, J. T., & Zhou, Q. (2013). Pressure buildup and
1138 brine migration during CO₂ storage in multilayered aquifers. *Ground*
1139 *Water*, 51(2), 252-267.
- 1140 Cottin, C., Bodiguel, H., & Colin, A. (2010). Drainage in two-dimensional
1141 porous media: from capillary fingering to viscous flow. *Phys. Rev. E*,
1142 82 (4), 046315.
- 1143 Cottin, C., Bodiguel, H., & Colin, A. (2011). Influence of wetting
1144 conditions on drainage in porous media: A microfluidic study. *Phys.*
1145 *Rev. E*, 84(2), 026311.
- 1146 DeHoff, K. J., Oostrom, M., Zhang, C., & Grate, J. W. (2012). Evaluation
1147 of two-phase relative permeability and capillary pressure relations
1148 for unstable displacements in a pore network, *Vadose Zone J.*, 11(4),
1149 doi:10.2136/vzj2012.0024.
- 1150 Doughty, C. (2010). Investigation of CO₂ Plume Behavior for a Large-
1151 Scale Pilot Test of Geologic Carbon Storage in a Saline Formation.
1152 *Transp. Porous Media*, 82 (1), 49-76.
- 1153 Dong, B., Yan, Y., & Li, W. (2011). LBM simulation of viscous fingering
1154 phenomenon in immiscible displacement of two fluids in porous
1155 media. *Transp. Porous Media*, 88(2), 293-314.
- 1156 Fathi, S. J., Austad, T., & Strand, S. (2010). Wettability Alteration in
1157 Carbonates: The Effect of Water-Soluble Carboxylic Acids in Crude
1158 Oil. *Energ. Fuels*, 24, 2514- 2519.
- 1159 Ferer, M., Ji, C., Bromhal, G. S., Cook, J., Ahmadi, G., & Smith, D. H.

1160 (2004). Crossover from capillary fingering to viscous fingering for
1161 immiscible unstable flow: Experiment and modeling. *Phys. Rev. E*,
1162 70 (1), 016303.

1163 Goodwin, D. G., Xia, Z., Gordon, T. B., Gao, C., Bouwer, E. J., &
1164 Fairbrother, D. H. (2016). Biofilm development on carbon nanotube/
1165 polymer nanocomposites. *Environ. Sci.: Nano*, 3, 475-684.

1166 Goodman, A., Hakala, A., Bromhal, G., Deel, D., Rodosta, T., Frailey, S.,
1167 Small, M., Allen, D., Romanov, V., Fazio, J., et al. (2011). U.S. DOE
1168 methodology for the development of geologic storage potential for
1169 carbon dioxide at the national and regional scale. *Int. J. Greenhouse*
1170 *Gas Control*, 5 (4), 952–965.

1171 Griбанова, E.; Molchanova, L.; Grigorov, O.; Porova, V. pH dependence
1172 of contact angles on glass and quartz. *Colloid J. USSR* 1976, 38,
1173 504–506.

1174 Hildebrand, T., & Rüesgsegger, P. (1996). A new method for the model-
1175 independent assessment of thickness in three-dimensional images. *J*
1176 *of Microscopy*, 185, 67–75.

1177 Hilfer, R., & Øren, P. E. (1996). Dimensional analysis of pore scale and
1178 field scale immiscible displacement. *Transp. Porous Med.*, 22, 53-
1179 72.

1180 Hu, R., Wan, J., Kim, Y., & Tokunaga, T. K. (2017a). Wettability effects
1181 on supercritical CO₂-brine immiscible displacement during drainage:

1182 Pore-scale observation and 3D simulation, *Int. J. Greenhouse Gas*
1183 *Control*, 60, 129-139.

1184 Hu, R., Wan, J., Kim, Y., & Tokunaga, T. K. (2017b). Wettability impact
1185 on supercritical CO₂ capillary trapping: Pore-scale visualization and
1186 quantification, *Water Resour. Res.* **2017b**, 53, 6377-6394,
1187 doi:10.1002/2017WR020721.

1188 Huq, F., Haderlein, S. B., Cirpka, O. A., Nowak, M., Blum, P., &
1189 Grathwohl, P. (2015). Flow-through experiments on water-rock
1190 interactions in a sandstone caused by CO₂ injection at pressures
1191 and temperatures mimicking reservoir conditions. *Appl. Geochem.*,
1192 58, 136-146

1193 Iglauer, S., Pentland, C., Bush, A. (2015). CO₂ wettability of seal and
1194 reservoir rocks and the implications for carbon geosequestration.
1195 *Water Resour. Res.*, 51, 729-774.
1196 <https://doi.org/10.1002/2014WR015553>.

1197 IPCC. (2005). Special report on carbon dioxide capture and storage. In:
1198 Metz, B., Davidson, O., de Coninck, H.C., Loos, M., Meyer, L.A. (Eds.),
1199 Prepared by Working Group III of the Intergovernmental Panel on
1200 Climate Change. Cambridge University Press, Cambridge, United
1201 Kingdom and New York, NY, USA.

1202 Juanes, R., MacMinn, C. W., & Szulczewski, M. L. (2010). The footprint
1203 of the CO₂ plume during carbon dioxide storage in saline aquifers:
1204 Storage efficiency for capillary trapping at the basin scale. *Transp.*
1205 *Porous Media*, 82 (1), 19-30.

1206 Jung, J. W., & Wan, J. (2012). Supercritical CO₂ and ionic strength
1207 effects on wettability of silica surfaces: Equilibrium contact angle
1208 measurements. *Energ. Fuels*, 26(9), 6053–6059.
1209 <https://doi.org/10.1021/ef300913t>.

1210 Kataok, I., Ishii, M., Serizawa, A. (1986). Local formulation and
1211 measurements of interfacial area concentration in two-phase flow.
1212 *Int. J. Multiph.*, 12 (4), 505–529.

1213 Karadimitriou, K. N., Mahani, H., Steeb, H. & Joekar-Niasar, V. (2019).
1214 Non-monotonic effects of salinity on wettability alteration and two-
1215 phase flow dynamics in PDMS micromodels. *Water Resour. Res.*,
1216 <https://doi.org/10.1029/2018WR024252>.

1217 Kim, Y., Wan, J., Kneafsey, T. J., & Tokunaga, T. K. (2012). Dewetting of
1218 silica surfaces upon reactions with supercritical CO₂ and Brine: Pore
1219 scale studies in micromodels. *Environ. Sci. Technol.*, 46 (7),
1220 4228–4235.

1221 Kovscek, A. R., Wong, H., & Radke, C. J. (1993). A pore-level scenario
1222 for the development of mixed wettability in oil reservoirs. *AIChE J.*,
1223 39, 1072–1085. <https://doi.org/10.1002/aic.690390616>.

1224 Krevor, S. C. M., Pini, R., Li, B., & Benson, S. M. (2011). Capillary
1225 heterogeneity trapping of CO₂ in a sandstone rock at reservoir
1226 conditions. *Geophys. Res. Lett.*, 38, L15401,
1227 [doi:10.1029/2011GL048239](https://doi.org/10.1029/2011GL048239).

1228 Levine, J. S., Goldberg, D. S., Lackner, K. S., Matter, J. M., Supp, M. G.,
1229 & Ramakrishnan, T. S. (2014). Relative permeability experiments of
1230 carbon dioxide displacing brine and their implications for carbon
1231 sequestration, *Environ. Sci. Technol.*, 48(1), 811-818.

1232 Lenormand, R., Touboul, E., & Zarcone, C. (1988). Numerical models
1233 and experiments on immiscible displacements in porous media. *J.*
1234 *Fluid Mech.*, 189, 165-187.

1235 Liu, H., Valocchi, A. J., Kang, Q., & Werth, C. (2013). Pore-scale
1236 simulations of gas displacing liquid in a homogeneous pore network
1237 using the Lattice Boltzmann method, *Transp. Porous Media*, 99(3),
1238 555-580.

1239 Lv, P., Liu, Y., Wang, Z., Liu, S., Jiang, L., Chen, J., & Song, Y. (2017). In
1240 Situ local contact angle measurement in a CO₂-brine-sand system
1241 using microfocused X-ray CT. *Langmuir*, 33, 3358-3366.

1242 MacMinn, C. W., Szulczewski, M. L., & Juanes, R. (2010). CO₂ migration
1243 in saline aquifers. Part 1. Capillary trapping under slope and
1244 groundwater flow. *J. Fluid Mech.*, 662 (7), 329-351.

1245 MacMinn, C. W., Szulczewski, M. L., & Juanes, R. (2011). CO₂ migration
1246 in saline aquifers. Part 2. Capillary and solubility trapping. *J. Fluid*
1247 *Mech.*, 688, 321-351.

1248 Moebius, F., & Or, D. (2014). Pore scale dynamics underlying the
1249 motion of drainage fronts in porous media. *Water Resour. Res.*, 50,
1250 8441-8457.

1251 Morrow, N. R. (1990). Wettability and its effect on oil recovery. *J. Petrol.*
1252 *Technol.*, 42 (12), 1476–1484.

1253 Nordbotten, J. M., Celia, M. A., & Bachu, S. (2005). Injection and
1254 Storage of CO₂ in Deep Saline Aquifers: Analytical Solution for CO₂
1255 Plume Evolution During Injection. *Transp. Porous Media*, 58 (3), 339–
1256 360.

1257 Park, D. S., Upadhyay, J., Singh, V., Thompson, K. E., & Nikitopoulos, D.
1258 E. (2015). Fabrication of 2.5D Rock-Based Micromodels with High
1259 Resolution Features. *ASME 2015 International Mechanical*
1260 *Engineering Congress and Exposition*, p V010T13A014.

1261 Pini, R., Krevor, S. C. M., & Benson, S. (2012). Capillary pressure and
1262 heterogeneity for the CO₂/water system in sandstone rocks at
1263 reservoir conditions. *Adv. Water Resour.*, 38, 48–59.

1264 Rasband, W. S. (1997–2019). ImageJ, U.S. National Institutes of Health,
1265 Bethesda, Maryland, USA, <https://imagej.nih.gov/ij/>.

1266 Rücker, M., Bartels, W. B., Singh, K., Brussee, N., Coorn, A., van der
1267 Linde, H. A., Bonnín, A., Ott, H., Hassanizadeh, S. M., Blunt, M. J.,
1268 Mahani, H., Georgiadis, A., & Berg, S. (2019). The effect of mixed
1269 wettability on pore-scale flow regimes based on a flooding
1270 experiment in Ketton limestone. *Geophys. Res. Lett.*, 46, 3225–
1271 3234. <https://doi.org/10.1029/2018GL081784>.

1272 Saffman, P. G., & Taylor, G. (1958). The penetration of a fluid into a
1273 porous medium or Hele-Shaw cell containing a more viscous liquid.
1274 *Proc. R. Soc. A*, 245, 312-329.

1275 Salathiel, R. A. (1973). Oil recovery by surface film drainage in mixed-
1276 wettability rocks. *J. Petrol. Technol.*, 25, 1216-1224.

1277 Sanchez-Vila, X., Dentz, M., & Donado, L. D. (2007). Transport-
1278 controlled reaction rates under local non-equilibrium conditions,
1279 *Geophys. Res. Lett.*, 34,L10404, doi:10.1029/2007GL029410.

1280 Seyyedi, M., Sohrabi, M., & Farzaneh, A. (2015). Investigation of rock
1281 wettability alteration by carbonated water through contact angle
1282 measurements. *Energ. Fuels*, 29, 5544-5553.

1283 Senel, O., Will, R., & Butsch, R. J. (2014). Integrated reservoir modeling
1284 at the Illinois Basin - Decatur Project. *Greenhouse Gases: Sci.*
1285 *Technol.*, 4 (5), 662-684.

1286 Shi, J. Q., Xue, Z., & Durucan, S. (2011). Supercritical CO₂ core flooding
1287 and imbibition in Tako sandstone-influence of sub-core scale
1288 heterogeneity *Int. J. Greenhouse Gas Control*, 5, 75-87.

1289 Tokunaga, T. K., Wan, J., Jung, J. W., Kim, T. W., Kim, Y., & Dong, W.
1290 (2013). Capillary pressure and saturation relations for supercritical
1291 CO₂ and brine in sand: High-pressure $P_c(S_w)$ controller/meter
1292 measurements and capillary scaling predictions, *Water Resour.*
1293 *Res.*, 49, 4566-4579, doi:10.1002/wrcr.20316.

1294 Trevisan, L., Pini, R., Cihan, A., Birkholzer, J. T., Zhou, Q., Gonzalez-
1295 Nicolas, A., & Illangasekare, T. H. (2017). Imaging and quantification
1296 of spreading and trapping of carbon dioxide in saline aquifers using
1297 meter-scale laboratory experiments. *Water Resour. Res.*, 53 (1),
1298 485-502, doi:10.1002/2016WR019749.

1299 Tsang, C. F., Birkholzer, J., Rutqvist, J. (2008). A comparative review of
1300 hydrologic issues involved in geologic storage of CO₂ and injection
1301 disposal of liquid waste, *Environ. Geol.*, 54, 1723-1737, doi:10.1007/
1302 s00254-007-0949-6.

1303 Tsakiroglou, C. D., & Avraam, D. G. (2002). Fabrication of a new class
1304 of porous media models for visualization studies of multiphase flow
1305 processes. *J. Mater. Sci.*, 37, 353. doi:10.1023/A:1013660514487.

1306 Wan, J., Tokunaga, T. K., Tsang, C. F., Bodvarsson, G. S. (1996).
1307 Improved glass micromodel methods for studies of flow and
1308 transport in fractured porous media, *Water Resour. Res.*, 32, 1955-
1309 1964.

1310 Wang, S., & Tokunaga, T. K. (2015). Capillary pressure-saturation
1311 relations for supercritical CO₂ and brine in limestone/dolomite
1312 sands: Implications for geologic carbon sequestration in carbonate
1313 reservoirs. *Environ. Sci. Technol.*, 49, 7208-7217.

1314 Wang, S., Edwards, I. M., Clarens, A. F. (2013), Wettability phenomena
1315 at the CO₂-brine-mineral interface: Implications for geologic carbon
1316 sequestration, *Environ. Sci. Technol.*, 47(1), 234-241.

1317 Wang, Y., Zhang, C., Wei, N., Oostrom, M., Wietsma, T. W., Li, X., &
1318 Bonneville, A. (2012). Experimental study of crossover from
1319 capillary to viscous fingering for supercritical CO₂-water
1320 displacement in a homogeneous pore network. *Environ. Sci.*
1321 *Technol.*, 47, 212-218.

1322 Xu, B., Yortsos, Y. C., & Salin, D. (1998). Invasion percolation with
1323 viscous forces. *Phys. Rev. E*, 57, 739-751.

1324 Xu, K., Bonnecaze, R., & Balhoff, M. (2017a). Egalitarianism among
1325 bubbles in porous media: an ostwald ripening derived
1326 anticoarsening phenomenon. *Phys. Rev. Lett.*, 119 (26), 264502.

1327 Xu, K., Liang, T., Zhu, P., Qi, P., Lu, J., Huh, C., & Balhoff, M. (2017b). A
1328 2.5-D glass micromodel for investigation of multi-phase flow in
1329 porous media. *Lab Chip*, 17, 640-646.

1330 Yang, D. Y., Gu, Y. G., & Tontiwachwuthikul, P. (2008). Wettability
1331 determination of the reservoir brine-reservoir rock system with
1332 dissolution of CO₂ at high pressures and elevated temperatures.
1333 *Energ. Fuels*, 22 (1), 504-509.

1334 Yun, W., Ross, C.M., Roman, S., & Kovscek, A. R. (2017). Creation of a
1335 dual-porosity and dual-depth micromodel for the study of
1336 multiphase flow in complex porous media. *Lab Chip*, 17 (8),
1337 1462-1474.

1338 Zarikos, I. M., Hassanizadeh, S. M., van Oosterhout, L. M., & van Oordt,
1339 W. (2018). Manufacturing a Micromodel with Integrated Fibre Optic

1340 Pressure Sensors. *Transp. Porous Media*,
1341 <https://doi.org/10.1007/s11242-018-1202-3>.

1342 Zhao, B., MacMinn, C. W., & Juanes, R. (2016). Wettability control on
1343 multiphase flow in patterned microfluidics. *Proc. Natl. Acad. Sci.*
1344 *U.S.A.*, 113 (37), 10251–10256.

1345 Zhang, C., Oostrom, M., Grate, J. W., Wietsma, T. W., & Warner, M. G.
1346 (2011a). Liquid CO₂ displacement of water in a dual-permeability
1347 pore network micromodel. *Environ. Sci. Technol.*, 45 (17), 7581–
1348 7588.

1349 Zhang, C., Oostrom, M., Wietsma, T. W., Grate, J. W., & Warner, M. G.
1350 (2011b). Influence of Viscous and Capillary Forces on Immiscible
1351 Fluid Displacement: Pore-Scale Experimental Study in a Water-Wet
1352 Micromodel Demonstrating Viscous and Capillary Fingering. *Energ.*
1353 *Fuels*, 25 (8), 3493–3505.

1354 Zheng, X., Mahabadi, N., Yun, T. S., & Jang, J. (2017). Effect of capillary
1355 and viscous force on CO₂ saturation and invasion pattern in the
1356 microfluidic chip. *J. Geophys. Res. Solid Earth*, 122, 1634–1647.

1357 Zhou, Q., & Birkholzer, J. T. (2011). On scale and magnitude of
1358 pressure build-up induced by large-scale geologic storage of CO₂.
1359 *Greenhouse Gases: Sci. Technol.*, 1(1), 11–20.

1360 Zuo, L., Zhang, C., Falta, R. W., & Benson, S. M. (2013). Micromodel
1361 investigations of CO₂ exsolution from carbonated water in
1362 sedimentary rocks. *Adv. Water Resour.*, 53, 188–197.

